

13. P. Kestler, in *Environmental Physiology and Biochemistry of Insects*, K. H. Hoffmann, Ed. (Springer-Verlag, Berlin, 1985), pp. 137–186.
14. Because water and CO<sub>2</sub> were removed from room air, the ambient partial pressure for CO<sub>2</sub> and water vapor was close to zero within the respirometric chamber. Pressure measurements inside the chamber yielded normal barometric pressure, and thus ambient partial pressure for O<sub>2</sub> amounted to ~20.95 kPa. Partial pressure for saturated water vapor is 3.29 kPa measured at 25°C (27).
15. The effective diffusion coefficient in air is 0.165 cm<sup>2</sup> s<sup>-1</sup> (for CO<sub>2</sub>), 0.209 cm<sup>2</sup> s<sup>-1</sup> (for O<sub>2</sub>), and 0.251 cm<sup>2</sup> s<sup>-1</sup> (for water vapor) at 25°C (28). The capacitance coefficient of CO<sub>2</sub>, O<sub>2</sub>, and water vapor in air is 410.5 nmol cm<sup>-3</sup> kPa<sup>-1</sup> measured at a pressure of 101.3 kPa and at 20°C (13).
16. The characteristic length and thus the point in the tracheal system at which internal partial pressure estimates apply was approximated at maximum water-loss rate and assuming that all spiracles are completely open. Equation 2 then yields a characteristic length of about 111 ± 14 μm (mean ± SD). The thorax width of *D. melanogaster* is ~0.8 mm.
17. G. Manning, M. A. Krasnow, in *The Development of Drosophila melanogaster*, M. Bate, A. M. Arias, Eds. (Cold Spring Harbor Laboratory Press, Cold Spring Harbor, NY, 1993), pp. 609–686.
18. P. L. Miller, *J. Exp. Biol.* **45**, 285 (1966).
19. Mean induced air velocity in the wake behind the two beating wings was estimated from the Rankine-Froude axial momentum theory that determines the air velocity from the momentum flux of air required to provide a given flight force. In the simplest case the wake is considered as a steady-state jet through an actuator disk with a uniform distribution of air velocities. Mean induced velocity,  $w_0$ , close to the stroke plane is given by the equation  $w_0 = (\frac{1}{2} F \rho^{-1} A_0^{-1})^{0.5}$ , in which  $F$  is total flight force,  $\rho$  is the density of the air, and  $A_0$  is the area swept by the two beating wings. Due to wake constriction, the theory shows that in the “far” wake the active area is solely  $\frac{1}{2} A_0$  whereas induced velocity reaches  $2w_0$  (29). Direct measurements of induced air velocity in the wake behind tethered flying fruit flies that responded to optomotor lift stimuli showed alterations in peak air velocity ranging from 0.88 at low flight forces to 0.94 m s<sup>-1</sup> at maximum force production (30).
20. W. P. Chan, M. H. Dickinson, *J. Exp. Biol.* **199**, 2767 (1996).
21. The Reynolds number ( $Re$ ) for tracheal air flow was approximated with a conventional model for flow in pipes that is given by  $Re = u d \nu^{-1}$  (28). In this equation  $u$  is flow velocity,  $d$  is the pipe diameter, and  $\nu$  is the kinematic viscosity of air. To derive an upper estimate of  $Re$ , I assumed Bernoulli ventilation of the tracheas at maximum induced air-flow velocity of 0.94 m s<sup>-1</sup> (79). The tracheal diameter was set to the maximum opening area of the large thoracic spiracles of ~42.5 μm. At a kinematic viscosity for air of  $15 \times 10^{-6}$  m<sup>2</sup> s<sup>-1</sup> (20°C),  $Re$  for tracheal air flow is about 2.7.
22. In *D. melanogaster*, the four thoracic spiracles form oval openings at the surface of about 60 μm by 25 μm each, whereas the circular openings of the 14 smaller abdominal spiracles are about 5 μm in diameter (17). From these values I calculated a total cross-sectional area of thoracic and abdominal openings of 5675 and 275 μm<sup>2</sup>, respectively. Assuming that only thoracic spiracles contribute to respiratory gas exchange, the given estimates for internal partial gas pressure would slightly change by ~5%.
23. Direct recordings of oxygen partial pressure in the flight muscle of large sweetpotato hawkmoths *Agrius convolvuli* made with microelectrodes have shown that internal oxygen concentration remains constant during the transition from rest to flight (31). Although large moths probably primarily use variation in tracheal convection to achieve stable internal partial pressure of respiratory gases, the finding suggests that constant partial pressure for oxygen might be preserved across even disparate insect species.
24. T. Weis-Fogh, *J. Exp. Biol.* **41**, 229 (1964).
25. The derived measures for overall tracheal conductance, internal partial gas pressure, and mean

opening area of the spiracles appear to be consistent with at least three different basic mechanisms of spiracle control. The fly may achieve an average tracheal conductance either by (i) matching the opening area of each spiracle to the respiratory needs, (ii) closing some spiracles while other spiracles remain open, or (iii) dynamically closing and opening the spiracles over time. Although all mechanisms could give similar mean tracheal conductance within the 100-ms time period used by the gas analyzer, periodically closing spiracles might increase the variance of tracheal partial pressures at a given flight force. Moreover, assuming that the spiracles ensure rather homogenous levels of oxygen throughout the active flight-muscle tissue, it seems unlikely that some thoracic spiracles are completely closed whereas others are completely open during flight.

26. R. Ziegler, in *Environmental Physiology and Biochemistry of Insects*, K. H. Hoffmann, Ed. (Springer-Verlag Berlin, 1985), pp. 95–118.
27. C. Gerthsen, H. Vogel, *Physik* (Springer-Verlag, Berlin, 1993), p. 238.
28. M. W. Denny, *Air and Water: The Biology and Physics*

of *Life's Media* (Princeton Univ. Press, Princeton, NJ, 1993), pp. 70–89.

29. C. P. Ellington, *Philos. Trans. R. Soc. London Ser. B* **305**, 115 (1984).
30. F.-O. Lehmann, thesis, University of Tübingen, Germany (1994).
31. Y. Komai, *J. Exp. Biol.* **201**, 2359 (1998).
32. T. B. Nikam, V. V. Khole, *Insect Spiracular Systems* (Halsted, New York, 1989).
33. Real-time fractional opening of the mesothoracic spiracle during flight was derived from intensity changes of light that was focused on the spiracle entrance by using small fiber optics. The amount of light reflected by the moving spiracular lids and thus the brightness of the spiracle's video image was greatest when the lids completely covered the spiracle entrance. Video images for calibration and data analysis were taken at 60-Hz sampling frequency with a conventional video camera.
34. I thank M. H. Dickinson for reading an early version of this manuscript. Supported by grants from the German Science Foundation (Le-905/4) and BMBF (Bio-Future 0311885).

27 July 2001; accepted 23 October 2001

## Real-Time Single-Molecule Imaging of the Infection Pathway of an Adeno-Associated Virus

Georg Seisenberger,<sup>1</sup> Martin U. Ried,<sup>2</sup> Thomas Endreß,<sup>1</sup> Hildegard Büning,<sup>2</sup> Michael Hallek,<sup>2,3</sup> Christoph Bräuchle<sup>1\*</sup>

We describe a method, based on single-molecule imaging, that allows the real-time visualization of the infection pathway of single viruses in living cells, each labeled with only one fluorescent dye molecule. The tracking of single viruses removes ensemble averaging. Diffusion trajectories with high spatial and time resolution show various modes of motion of adeno-associated viruses (AAV) during their infection pathway into living HeLa cells: (i) consecutive virus touching at the cell surface and fast endocytosis; (ii) free and anomalous diffusion of the endosome and the virus in the cytoplasm and the nucleus; and (iii) directed motion by motor proteins in the cytoplasm and in nuclear tubular structures. The real-time visualization of the infection pathway of single AAVs shows a much faster infection than was generally observed so far.

Single-molecule detection techniques have been developed for imaging and for spectroscopic characterization of individual fluorescent molecules (1–3). Within the last years, these techniques have been increasingly applied to biological topics (4, 5). By overcoming the problem of ensemble averaging, these techniques enabled questions in molecular biology to be solved, which hitherto could not be an-

swered by conventional ensemble measurements (6–8). Single-molecule imaging has previously been applied to study the diffusional behavior of single molecules in lipid bilayers (9, 10), in fluids (11–13), or recently, in living cells (14) and their membranes (15, 16). Here, we show for the first time that this method can be used for the visualization and kinetic characterization of the infection pathway of single viruses in living cells.

The viral infection process is a very intriguing interaction in nature. It starts with the contact between the virus and the cell membrane and finally results in transport of the virus into the nucleus and gene expression. For antiviral drug design, as well as for the development of efficient gene therapy vectors, it is essential to understand these processes. Electron microscopy is one tool for obtaining knowledge on the

<sup>1</sup>Department Chemie, Ludwig-Maximilians-Universität München, Butenandtstraße 11, D-81377 München, Germany. <sup>2</sup>Genzentrum, Laboratorium für Molekulare Biologie, Medizinische Klinik III, Klinikum Großhadern, Ludwig-Maximilians-Universität München, Feodor-Lynen-Straße 25, D-81377 München, Germany. <sup>3</sup>GSF—National Center for Research and Environment, KKG Genterapie, Marchioninistraße 25, D-81377, Germany.

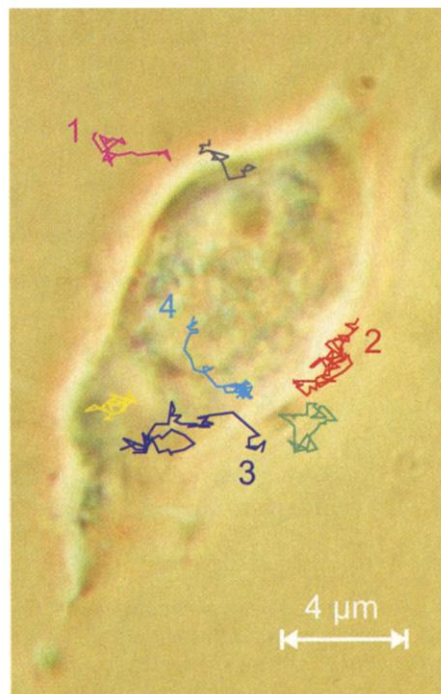
\*To whom correspondence should be addressed. E-mail: christoph.braeuchle@cup.uni-muenchen.de

different stages of the infection pathway, but it cannot be carried out in living cells with high time resolution (17). A first step in this direction was the establishment of capsid labeling methods and their detection in fixed cells by conventional fluorescent microscopy (18). However, using conventional fluorescent microscopy either a high concentration of viruses or a high degree of labeling or both had to be used. This masks the detection of individual processes, can create unphysiological conditions, altering the kinetics of the infection process, and due to steric hindrance can inter-

fere with the virus-cell interaction. In this regard, real-time imaging of single viruses labeled with only one dye molecule in living cells is a breakthrough.

Our model system AAV is a promising vector for gene therapy (19), although its infection process is still not completely understood (20, 21). For this study, AAV was covalently labeled with Cy5 dye, with a ratio of single to double labeling of 82:18. We analyzed 1009 trajectories of single AAV-Cy5 particles in 74 cells at different stages of the infection, an example of which is shown in Fig. 1.

**Fig. 1.** Trajectories of single AAV-Cy5 particles indicating infectious entry pathways of AAVs into a living HeLa cell. To demonstrate how cell constituents were determined, trajectories are projected onto a phase contrast image of the investigated cell cross-section, taken with a commercial CCD (Coolpix, Nikon) attached to the binocular tubus of the microscope (36). The traces showing single diffusing virus particles were recorded at different times. They describe various stages of AAV infection, e.g. diffusion in solution (1 and 2), touching at the cell membrane (2), penetration of the cell membrane (3), diffusion in the cytoplasm (3 and 4), penetration of the nuclear envelope (4), and diffusion in the nucleoplasm. Under excitation with red light (633 nm) the autofluorescence of cells was low enough to allow the observation of single fluorophores as bright spots (Fig. 3, A and B). A two-dimensional gaussian fit of the intensity profile (9, 10) provided a localization accuracy of 40 nm for these spots. We took series of images at 40 ms intervals to construct two-dimensional projections of single AAV-Cy5 trajectories. The brightness of the fluorescence spots in these series shows the time dependence of the fluorescence intensity (see fluorescence time traces in Fig. 3, C through E).



The motion of AAV outside the cell could be characterized as normal diffusion with a diffusion coefficient of  $D = 7.5 \mu\text{m}^2/\text{s}$  (22).

When AAV approached the cell membrane, a general deceleration was observed (23). Typical trajectories displayed (Figs. 1 and 2A) movements toward the cell surface, followed by a mean of 4.4 repetitive touching events (Fig. 2B) with a mean touching time of  $t_t = 62 \text{ ms}$  (Fig. 2C), interrupted by short diffusion paths in the vicinity of the cell surface. It is not clear yet, whether these touching events represent binding/release processes at a receptor or simply unpecific adsorption of the virus to the cell surface. The touching resulted in a mean contact time of  $t_c = 3.2 \text{ s}$ , measured between the first and the last cell surface contact. For virus particles that entered a cell, the mean contact time decreased to  $t_c = 1.2 \text{ s}$ , because the series of touching events was stopped by penetration of the membrane. A penetration efficiency of 13% was measured (24), implying that the membrane itself is a major barrier for virus uptake. The precise reason for this phenomenon is unknown, but probably involves a failure of interaction of receptor and different cofactors essential for the virus internalization (25–27).

The postulated uptake mechanism for AAV into living cells requires endocytosis (20, 21). To our surprise, adsorption times at the cell membrane for particles which penetrated cells were not increased compared to those followed by detachment from the cell surface. These times are in the range of 64 ms, which is very short, especially for adsorption followed by penetration (Fig. 2D). First measurements on CHO K1 cells gave similar values. Nevertheless, there is strong evidence that the AAV entry pathway starts with endosome formation,

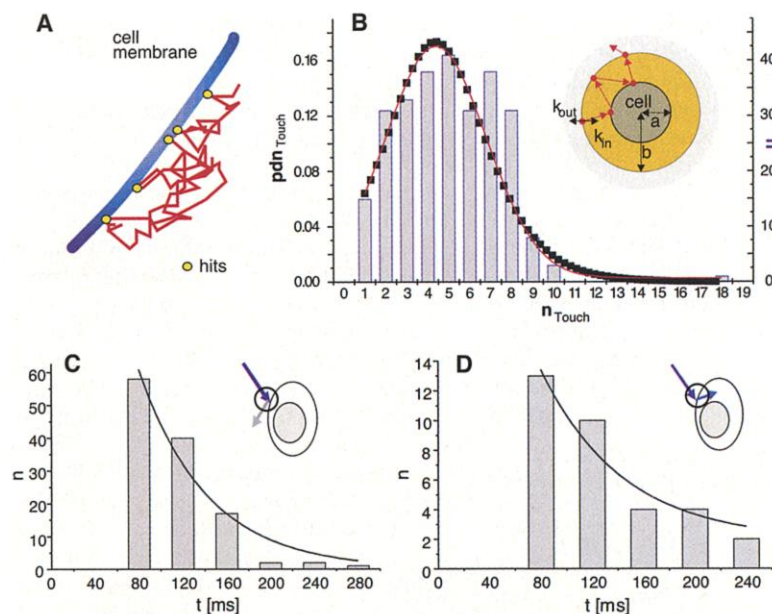


**Fig. 2.** Uptake of AAV-Cy5 by a living HeLa cell. (A) Membrane “touching events” of AAV at the surface of a living HeLa cell. An enlarged sketch of trajectory 2 taken from Fig. 1. The path shows five touches to the cell surface. These hits are highlighted by circles and represent short periods of immobility. (B) The mean number of consecutive cell touches  $\langle n_{\text{Touch}} \rangle$  derived for viruses with negative docking (diffusing back into solution) calculated from 269 trajectories (frequency plot with gray bars). The accumulated frequency of  $n_{\text{Touch}}$  was fitted with a sigmoid function. Its normalized derivative, the probability density function  $pdn_{\text{Touch}}$  (dot curve) was fitted with a gaussian curve. From this fit a mean value  $\langle n_{\text{Touch}} \rangle = 4.4 \pm 3.1$  was determined. A model for the statistical calculation of cell surface touches is inserted in (B) (37). In an idealized model the cell is seen as a spherical shell of radius  $r = a$ . Particles released at  $r = b$  move inward at a rate of  $k_{\text{in}}$  or outward with  $k_{\text{out}}$ . The probability  $p$  for touching the sphere is  $p = k_{\text{in}} / (k_{\text{in}} + k_{\text{out}}) = a/b$ . The mean number of consecutive touches a particle undergoes oscillating between  $r = a$  and  $r = b$  before wandering away from the shell for good is  $\langle n_{\text{Touch}} \rangle = \sum_{n=0}^{\infty} np^n(1-p) = p/(1-p) = a/(b-a)$ . This mean number can be estimated to be  $\langle n_{\text{Touch}} \rangle = 5$  for a typical value of  $a = 5 \mu\text{m}$  and a typical value of  $b = 6 \mu\text{m}$  between the touches. Distribution of adsorption times for 137 negative docking (C) and 42 membrane penetration (D) trajectories. The bars indicate the accumulated frequency of

viruses observed with specific docking times before leaving the cell surface or penetrating the cellular membrane. These accumulated frequencies are fitted with exponential functions. Based on these data, the 1/e decays of the docking times were determined to be  $\langle t \rangle = 62 \pm 30 \text{ ms}$  (C) and  $\langle t \rangle = 64 \pm 30 \text{ ms}$  (D), respectively, indicating no significant time differences between cell leaving and penetrating events.

## REPORTS

followed by virus release. We imaged 113 trajectories within the cytoplasm and analyzed their diffusion as discussed before (Fig. 3, A through G). Fifty-three trajectories showed a linear  $\langle r^2 \rangle - t$  movement indicating normal diffusion. The distribution function of the calculated diffusion constants (Fig. 3H) showed two maxima at  $D = 1.3 \mu\text{m}^2/\text{s}$  and  $D = 0.6 \mu\text{m}^2/\text{s}$ , indicating two different components. The faster species, which is approximately five times slower than the diffusion coefficient of AAV in aqueous solution, can be assigned to the free virus. The reduction of the diffusion coefficient matches the results known from other macromolecules diffusing in the cytoplasm (28, 29). Using the Stokes-Einstein equation, the slower component can be assigned to a particle of about 50 nm in diameter, which was identified as AAV inside an endosome. Control experiments done in cells at pH = 9 support this interpretation (Fig. 3I). In all experiments no free virus but only endosome diffusion has been observed directly after membrane penetration and only one virus per endosome was found.

Fifty-one trajectories showed deviations from the linear dependency of mean square displacement with time (Fig. 3, F and G), indicating anomalous diffusion processes ( $\langle r^2 \rangle = 4Dt^\alpha$ ) with a  $D$  value in the range of 0.3 to  $1.5 \mu\text{m}^2/\text{s}$  and  $0.5 < \alpha < 0.9$ . This kind of diffusion occurred in localized areas of the cell and can be ascribed to obstacles or adsorption sites hindering the free Brownian movement of the particles (30).

Furthermore, directed motion was observed for nine of the trajectories in the cytoplasm. For all these cases the mean square displacement could only be fitted with a parabola [ $r^2 = 4Dt + (vt)^2$ ] indicating diffusion with drift (30). The calculated diffusion coefficients were within the range of  $D = 0.4$  to  $0.9 \mu\text{m}^2/\text{s}$  and velocities in the range of  $v = 1.8$  to  $3.7 \mu\text{m}/\text{s}$ . Treatment with nocodazole started 1 hour before infection removed the directed motion, indicating microtubule-dependent transport of viruses by motor proteins like kinesin or dynein. This kind of transport mechanism is known to occur for several viruses which use it as an efficient

way to move toward the nucleus (17, 21, 31).

At 15 min after the start of the experiment (32), at least one AAV-Cy5 was detected in the nucleus of 50% of the cells. This indicates a much faster infection compared to the 2-hour infection time measured by Bartlett *et al.* (20) for the same system with conventional methods. Conventional methods require the accumulation of a higher number of viruses for detection; our method, which is sensitive to single viruses, gives much shorter and more accurate values.

More than a hundred trajectories of viral particles were measured in the nuclear area of cells with different sized nuclei. Fifty-seven of the trajectories showed normal diffusion, with diffusion coefficients ranging from  $D = 0.4$  to  $1.3 \mu\text{m}^2/\text{s}$  with a mean value of  $\langle D \rangle = 0.85 \mu\text{m}^2/\text{s}$ . In addition, for 23 of the viral particles anomalous diffusion was observed with  $D$  in the range of 0.1 to  $0.5 \mu\text{m}^2/\text{s}$  and  $0.6 < \alpha < 0.9$ . These values indicate a somewhat slower, but in principal, similar movement of viruses in the nuclear area as compared to the cytoplasm.

To our great surprise, in 34 of the trajecto-

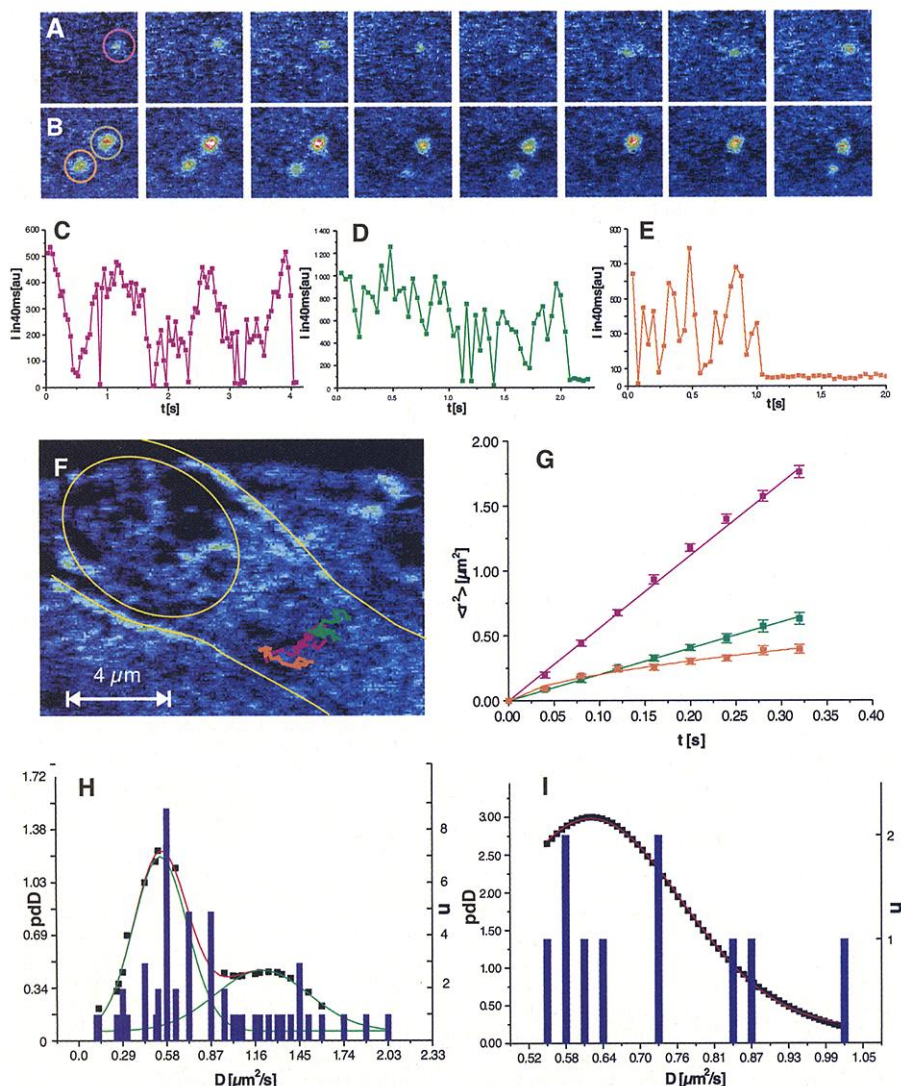


**Fig. 3.** Endosomal processing and diffusion in cytoplasm. (A and B) Two series of fluorescence images showing one and two fluorescence spots each indicating a single AAV particle. Time distance for each panel is 40 ms and the size is  $5 \mu\text{m}$  by  $5 \mu\text{m}$ . (C through E) Time traces of the fluorescence intensity (I) of the spots shown in (A) and (B) (correlated by color). The plots feature the characteristic on/off dynamics (blinking) and one-step photobleaching behavior typical of single molecules. Time trace noise is the result of diffusive movement perpendicular to the focal plane (38). (F) Visualization of the three trajectories projected onto the transmitted light image taken with the microscopic setup used for fluorescence detection. Cell membrane and nucleus, both outlined yellow, were determined by phase contrast imaging as demonstrated in Fig. 1. (G) The mean square displacement plotted with time. The magenta curve yielding a diffusion coefficient of  $D = 1.4 \mu\text{m}^2/\text{s}$  is ascribed to a free AAV particle undergoing normal diffusion in the cell plasma. The green and yellow curves are attributed to endosomal movements, one with normal diffusion ( $D = 0.55 \mu\text{m}^2/\text{s}$  green) and one with anomalous diffusion ( $D = 0.2 \mu\text{m}^2/\text{s}$ ,  $\alpha = 0.6$  yellow). (H and I) Probability density function pdD for diffusion coefficients derived for particle movement in the cytoplasm (obtained in analogy to Fig. 2B) from 53 trajectories at pH = 7 (H) and 10 trajectories at pH = 9 (I). We found two maxima of the probability density function for pH = 7 attributed to free AAV ( $D = 1.3 \mu\text{m}^2/\text{s}$ ) and to AAV inside the endosome ( $D = 0.57 \mu\text{m}^2/\text{s}$ ). The latter maximum is similar to the maximum ( $D = 0.64 \mu\text{m}^2/\text{s}$ ) found for pH = 9, at which endosomal release is not possible. The low value of  $D$  in (H) was therefore assigned to AAV inside an endosome. The histograms show the distribution of diffusional constants.

ries within the nuclear area the viral particles underwent directed motion along well-defined pathways (Fig. 4). Some pathways were used several times consecutively by different viral particles. In addition, all trajectories in a given nuclear area were “unidirectional,” i.e., oriented in roughly the same direction through the nuclear area (Fig. 4A). The typical number of pathways taken seems to be restricted to about one to five within one nuclear area. For all these trajectories, the mean square displacement was quadratically dependent on  $t$  (30), resulting in diffusion coefficients in the range of  $D = 0.25$  to  $0.9 \mu\text{m}^2/\text{s}$  and velocities in the range of  $v = 0.2$  to  $2.8 \mu\text{m}/\text{s}$ . Again, treatment with nocodazole prevented directed motion. This would suggest active transport of the virus within the nuclear area. However, motor proteins such as kinesin or dynein as well as microtubules have not been observed in the nucleoplasm so far. On the other hand, it is well known that tubular structures, formed by invagination of the nuclear envelope exist and

sometimes even transect the nucleus (33, 34). The core of these channels is continuous with the cytoplasm. Microtubules could polymerize into these channels and allow active transport of the AAV by motor proteins. This model would explain the observation of the typical number of pathways and the “unidirectional” movement described above, because (i) the typical number of large nuclear channels is one to five (33) and (ii) the growth of the microtubules have to start from the centrosome on one side of the nucleus, more or less “unidirectional” into the nuclear channels. If either kinesin or dynein are used as motor proteins, the “unidirectional” transport is comprehensible. It is remarkable to observe viruses diffusing freely in the cytoplasm and then suddenly starting to move with constant velocity into the nuclear area along well-defined pathways [real-time movie available at (35)].

In conclusion our single virus tracing measurements have allowed, for the first time, a detailed observation and quantitative description of the infectious entry pathway of single virus particles labeled with only one dye molecule into living cells. The low degree of labeling and the extremely low concentration of viruses per cell guaranteed natural and physiological conditions with a minimum of distortion of the virus-cell interactions in contrast to all measurements carried out so far. The presented experiments give a real-time movie script of a virus infection in a living human cell with a hitherto unachievable clarity and detail. Refinement of the method to include labeling of capsid and viral DNA with different dyes will further allow characterization of the disassembly and nuclear processing of viruses. Knowledge obtained by single virus tracing experiments as described here, will give new insight into the broad scale of virus-cell interactions and will be essential for the development of antiviral drugs and specific second generation gene therapy vectors.

References and Notes

1. S. Nie, R. N. Zare, *Annu. Rev. Biophys. Biomol. Struct.* **26**, 567 (1997).
2. X. S. Xie, J. K. Trautman, *Annu. Rev. Phys. Chem.* **49**, 441 (1998).
3. W. E. Moerner, M. Orrit, *Science* **283**, 1670 (1999).
4. S. Weiss, *Science* **283**, 1676 (1999).
5. Y. Ishii, T. Yanagida, *Single Mol.* **1**, 5 (2000).
6. T. Funatsu, Y. Harada, M. Tokunaga, K. Saito, T. Yanagida, *Nature* **374**, 555 (1995).
7. H. Noji, R. Yasuda, M. Yoshida, K. Kinosita Jr., *Nature* **386**, 299 (1997).
8. H. P. Lu, L. Xun, X. S. Xie, *Science* **282**, 1877 (1998).
9. T. Schmidt, G. J. Schütz, W. Baumgartner, H. J. Gruber, H. Schindler, *J. Phys. Chem.* **99**, 17662 (1995).
10. G. J. Schütz, H. Schindler, T. Schmidt, *Biophys. J.* **73**, 1073 (1997).
11. R. M. Dickson, D. J. Norris, Y. L. Tzeng, W. E. Moerner, *Science* **274**, 966 (1996).
12. X. H. Xu, E. S. Yeung, *Science* **275**, 1106 (1997).
13. U. Kubitschek, O. Kuckmann, T. Kues, R. Peters, *Biophys. J.* **78**, 2170 (2000).
14. M. Goulian, S. M. Simon, *Biophys. J.* **79**, 2188 (2000).

15. G. J. Schutz, G. Kada, V. P. Pastushenko, H. Schindler, *EMBO J.* **19**, 892 (2000).
16. Y. Sako, S. Minoguchi, T. Yanagida, *Nature Cell Biol.* **2**, 168 (2000).
17. B. Sodeik, M. W. Ebersold, A. Helenius, *J. Cell Biol.* **136**, 1007 (1997).
18. J. S. Bartlett, R. J. Samulski, *Nature Med.* **4**, 635 (1998).
19. R. M. Kotin, *Hum. Gene Ther.* **5**, 793 (1994).
20. J. S. Bartlett, R. Wilcher, R. J. Samulski, *J. Virol.* **74**, 2777 (2000).
21. S. Sanlioglu et al., *J. Virol.* **74**, 9184 (2000).
22. To characterize the motion of AAV outside the cell, we analyzed more than 500 individual displacement steps per time window in 80 AAV-Cy5 trajectories, with a distribution function for square displacements derived from the Fick's 2nd law of diffusion (10). We observed a linear dependence of mean square displacements with time ( $\langle r^2 \rangle = 4Dt$ ) indicative of free diffusion (30). The obtained diffusion coefficient of labeled AAV particles was  $D = 7.5 \mu\text{m}^2/\text{s}$ . This is in reasonable agreement with the calculated value ( $D = 11 \mu\text{m}^2/\text{s}$ ) derived from the Stokes Einstein equation for AAV assuming a spherical particle with a radius of  $r = 13 \text{ nm}$ .
23. First measurements with CHO K1 cells and CHO K1 heparan sulfate-negative cells (pgsA-745), show a similar behavior, indicating that other parts of the cell membrane, not the HSPG receptor, may be responsible for this effect. Further experiments are in progress to clarify this point.
24. In order to characterize the penetration efficiency, we determined the ratio of the number of penetration events to the overall number of membrane contact events. Of 847 trajectories starting outside the cell, 508 did not show any interaction with the cell. In 271 of the trajectories analyzed, the virus particle made membrane contact and then rediffused into the solution. Twenty-five of the particles stuck persistently to the cell membrane. Virus entry into the cell was seen in only 43 of the trajectories. This results in a penetration efficiency of only 13%.
25. C. Summerford, R. J. Samulski, *J. Virol.* **72**, 1438 (1998).
26. C. Summerford, J. S. Bartlett, R. J. Samulski, *Nature Med.* **5**, 78 (1999).
27. K. Qing et al., *Nature Med.* **5**, 71 (1999).
28. O. Seksek, J. Biwersi, A. S. Verkman, *J. Cell Biol.* **138**, 131 (1997).
29. K. Luby-Phelps, *Int. Rev. Cytol.* **192**, 189 (2000).
30. M. J. Saxton, K. Jacobson, *Annu. Rev. Biophys. Biomol. Struct.* **26**, 373 (1997).
31. M. Suomalainen et al., *J. Cell Biol.* **144**, 657 (1999).
32. The start of the experiment is defined here as adding the AAV solution to the sample with the cells.
33. M. Fricker, M. Hollinshead, N. White, D. Vaux, *J. Cell Biol.* **136**, 531 (1997).
34. J. L. Broers et al., *J. Cell Sci.* **112**, 3463 (1999).
35. www.single-virus-tracing.com.
36. Virus solution of AAV-Cy5 of low concentrations ( $10^{-9}$  to  $10^{-11} \text{ mol l}^{-1}$ ) was added to culture medium (Dulbecco's modified Eagle medium) of HeLa cells. This typically resulted in 10 to 1000 viral particles per cell. An area of  $20 \mu\text{m}$  by  $20 \mu\text{m}$  containing a single cell was imaged with an epifluorescent microscope using a  $100\times$  objective (Plan-Neofluar, NA 1.3, Zeiss) and a high-sensitivity charge-coupled device (CCD) camera system (Pentamax, Princeton Instruments).
37. H. C. Berg, *Random Walks in Biology* (Princeton Univ. Press, Princeton, NJ, ed. 10, 1993).
38. Cy5 molecules can undergo an average of  $10^6$  photocycles in buffer/agarose gel before photobleaching. In the experiments described here, the excitation intensity was carefully adjusted to achieve sufficient brightness for fluorescence detection, but also long trajectories before photobleaching. With a detection efficiency of about  $\epsilon = 1\%$  and a fluorescence-intensity per spot of several hundred counts, trajectories of 1 to 10 s could be obtained.
39. We are in debt to C. David for valuable discussions and careful reading of the manuscript together with A. Hards. Experimental support by A. Zumbusch, T. Hellerer, S. Grimm, N. Huttner, and M. Öhm is gratefully acknowledged.

5 July 2001; accepted 15 October 2001

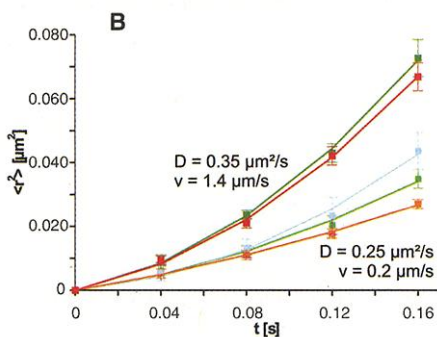
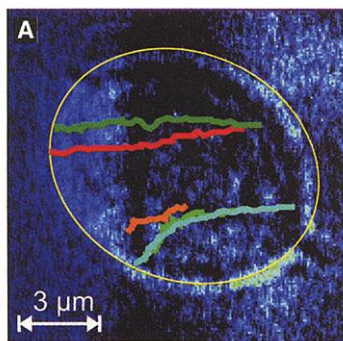


**Fig. 4.** Transport of AAV-Cy5 within the nuclear area. (A) The visualization of five trajectories projected onto the white light image of the cell nucleus. The position of the nucleus outlined in yellow was determined with phase contrast imaging. The lower two trajectories run along the same pathway consecutively. In this case, all trajectories showed directed motion from the left to the right side, i.e. were “unidirectional.” (B) Mean square displacement plotted with time. The parabolic shape of the curves indicates diffusion with drift as described by the equation  $\langle r^2 \rangle = 4Dt + (vt)^2$  with diffusion coefficients of  $D = 0.25$  to  $0.35 \mu\text{m}^2/\text{s}$  and velocities in the range of  $v = 0.2$  to  $1.4 \mu\text{m}/\text{s}$ .